Polymer Testing 102 (2021) 107316

Contents lists available at ScienceDirect

Polymer Testing

journal homepage: www.elsevier.com/locate/polytest

# Low-cost nanofabrication of isoporous nanomembranes using hybrid lithography

Akarapan Rojjanapinun [a], Sheree A. Pagsuyoin [a,*], Jason Perman [b], Hongwei Sun [c]

[a] Civil and Environmental Engineering, University of Massachusetts Lowell, Lowell, MA, USA
[b] Anton Paar QuantaTec Inc., 1900 Corporate Dr., Boynton Beach, FL, USA
[c] Mechanical Engineering, Northeastern University, Boston, MA, USA

ARTICLE INFO

*Keywords:*
Isoporous nanomembranes
Nanosphere lithography
Soft lithography
Nanoparticle monolayer

ABSTRACT

This work demonstrates an improved route to develop low-cost and robust isoporous polyvinylidene fluoride (PVDF) nanomembranes for industrial separation and purifications processes. The 4-step process excels at making uniform 100 nm and 20 nm pore membranes that exhibit high flux in both dead-end and cross-flow filtration. Our tests demonstrate that 90–100% rejection rates could be achieved in these membranes for perfluorooctanoic acid, sulfamethoxazole, bovine serum albumin, and SARS-COV-2 in high-concentration aqueous solutions. The membranes are nominally 50 μm thick and retain structural integrity, exhibiting high tensile strengths of 8.56 MPa and 8.31 MPa, respectively, due to improved routes to β crystalline formations of the PVDF. Our useful fabrication procedure is compatible with developed technologies that can quickly expand the opportunities of isoporous PVDF for processing of advanced materials and devices.

## 1. Introduction

Technological innovations continue to advance manufacturing techniques for membranes used in separation and purification processes [1,2], personal protective equipment [3], and medical devices [4]. For these applications, membranes should ideally be durable, highly permeable, resistant to fouling, and economical to manufacture. For specialized processes that require ultra- or nanomembranes, commercially available membranes are typically manufactured via track-etching [5], electrospinning [6], and phase inversion [7]. In track-etching, a polymer film is irradiated with charged ions, creating latent tracks on the film which are subsequently transformed into hollow channels by chemical etching [8]. This method can produce isoporous membranes but precise control of the ion bombardment process is needed to prevent overlapping tracks on the film [9]. In electrospinning, charged polymer solutions or melts are ejected out of a spinneret through the application of high-voltage electric field, producing fine fiber filaments that can be spun on a surface in specific patterns [10,11]. In phase inversion, the solvent in a liquid polymer solution is removed, leaving behind a solidified porous membrane [12]. The characteristic pore structure of the membrane is controlled by the solvent properties and solidification conditions, with recent techniques capable of producing pore structures in the 1–100 nm range [9].

Surface patterning via lithography has been demonstrated as an efficient technique for manufacturing low-cost yet durable membranes [13]. However, conventional techniques such as photolithography require a clean room to prevent the deposition of air-borne impurities on the polymer as it sets on the substrate surface [14]. Furthermore, highly sophisticated instrumentation (e.g., mask aligner, e-beam) may be required to etch patterns on the master mask, which limits its large scale use. Alternatively, membrane manufacture via soft lithography comprises sequential steps (Fig. 1): (i) fabrication of the master mask, (ii) fabrication of the soft elastomeric mold using the master mask, and (iii) fabrication of the membrane structures using the mold. In this study, we developed a novel and simple hybrid technique based on room temperature nanosphere lithography and soft lithography to fabricate thin film membranes with highly uniform nanopore structures (100 nm and 20 nm pore). Lei et al. [15] have previously demonstrated that polystyrene nanoparticles (PSN) can be assembled as a tightly packed monolayer on a water-air interface using dip-drop method. In the present work, a closely-packed monolayer of polystyrene nanosphere particles was overlain on an SU-8 substrate and etched with oxygen plasma to create the master mask. Soft lithography was used to manufacture polyvinylidene fluoride (PVDF) nanomembranes via stamping using a

* Corresponding author. Department of Civil and Environmental Engineering, University of Massachusetts Lowell, Lowell, MA, 01854, USA.
*E-mail address:* Sheree_Pagsuyoin@uml.edu (S.A. Pagsuyoin).

https://doi.org/10.1016/j.polymertesting.2021.107316
Received 20 May 2021; Received in revised form 28 July 2021; Accepted 19 August 2021
Available online 20 August 2021

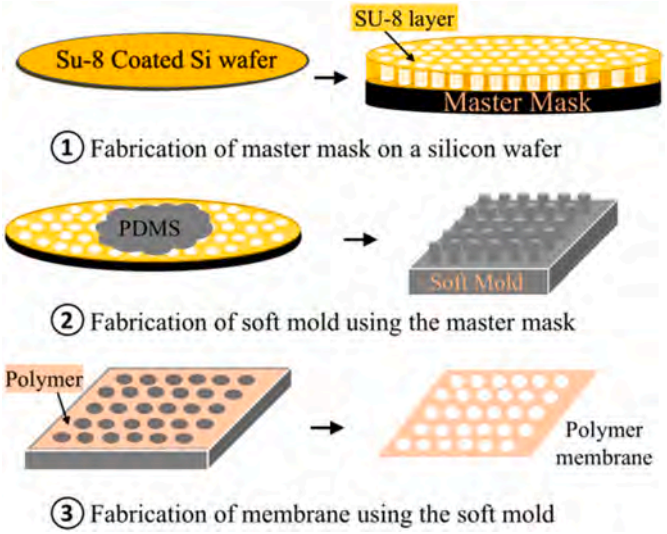


**Fig. 1.** The soft lithography process for membrane manufacture consists of sequential steps which include fabrication of the master mask, which is used to manufacture the elastomeric mold, which in turn is used to cast the polymer membrane.

polydimethylsiloxane (PDMS) mold. The mechanical properties and performance characteristics of the product membranes were also evaluated and compared with literature for similar membranes manufactured from other techniques. Membrane performance was evaluated via filtration of high concentration aqueous solutions of perfluorooctanoic acid (PFOA), sulfamethoxazole (SMX), bovine serum albumin (BSA), and heat-inactivated SARS-CoV-2.

## 2. Experimental

**Materials and chemicals.** Silicon wafer P-type with 100-mm diameter was obtained from University Wafer (MA, USA). The polystyrene nanoparticles (PSN, 200–300 nm diameter, as 10% w/v in DI water) was purchased from Spherotech (IL, USA). SU-8 3050 was purchased from MicroChem (MA, USA). Polyethylene oxide (PEO, 100 kDA) was purchased from Alfa Aesar (PA, USA). Polyvinylidene fluoride (PVDF, 530 kDa), polydimethylsiloxane (Sylgard-184), perfluorooctyltrichlorosilane (FOTS), N-methyl-2-pyrrolidone (NMP), ethyl alcohol (≥99.5%), sulfuric acid ($H_2SO_4$, 96%), hydrogen peroxide ($H_2O_2$, 30%), toluene (99.8%), chromium etchant standard (CR-20), methanol (99.8%), perfluorooctanoic acid and sulfamethoxazole standards, and bovine serum albumin were purchased from Sigma-Aldrich and were used as received. Ultrapure water was prepared using an onsite water purification system (Barnstead Easypure II). Heat-inactivated SARS-CoV-2 samples were provided by the Next Generation Sequencing Laboratory at the University of Massachusetts Lowell.

**Step 1: Preparation of SU-8 coated Si wafer**. The Si wafer was cleaned chemically with a piranha solution (3:1 v/v mixture of 18 M $H_2SO_4$ and 42.4 M $H_2O_2$) and then washed with ultrapure water. The cleaned wafer was heated at 180 °C overnight for complete dehydration and then gradually cooled to room temperature. A 50-μm-thick layer of SU-8 was coated on the wafer using a spin coater (3000 rpm for 80 s). The wafer was then exposed to UV light at an intensity of 10 mW/cm$^2$ for 20 min, then baked at 90 °C for 1 h on a hotplate and cooled to room temperature.

**Step 2: Preparation of closely-packed polystyrene nanosphere monolayer**. The preparation of the closely-packed PSN monolayer was carried out at room temperature following a previous procedure18 with modifications. To briefly describe, 800 mL of DI water was placed in a clean beaker and then ultrasonicated for 15 min to remove dissolved gases. The SU-8-coated Si wafer was then lowered horizontally into the beaker, then a thin polypropylene (PP) ring (diameter of 100 mm) was floated on the water surface to serve as a confinement area for the PSN. The PSN stock was mixed with ethanol at 2:1 vol ratio, and then added dropwise at 2 μL volume increments onto the water surface using an angled glass slide and a micropipette until the polypropylene ring was fully covered with PSN (Fig. 2). 4 mg of water-soluble polyethylene oxide (PEO) powder was then gradually sprinkled on the water surface to induce a PSN close-packed monolayer. After 2 h, the PSN layer was transferred to the surface of the SU-8-coated Si substrate by slowly draining the water at a flow rate of 5 mL/min using a peristaltic pump.

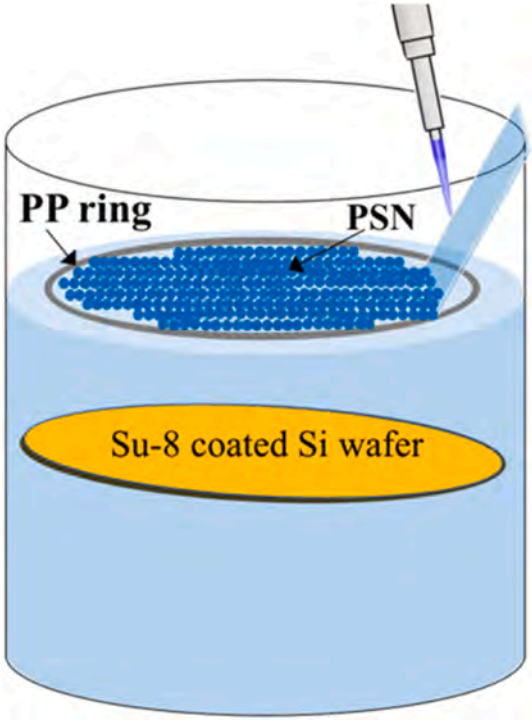


**Fig. 2.** Preparation of closely-packed PSN monolayer on Su-8-coated Si wafer via drop-wise addition of PSN in a polypropylene ring confined area using an angled glass slide.

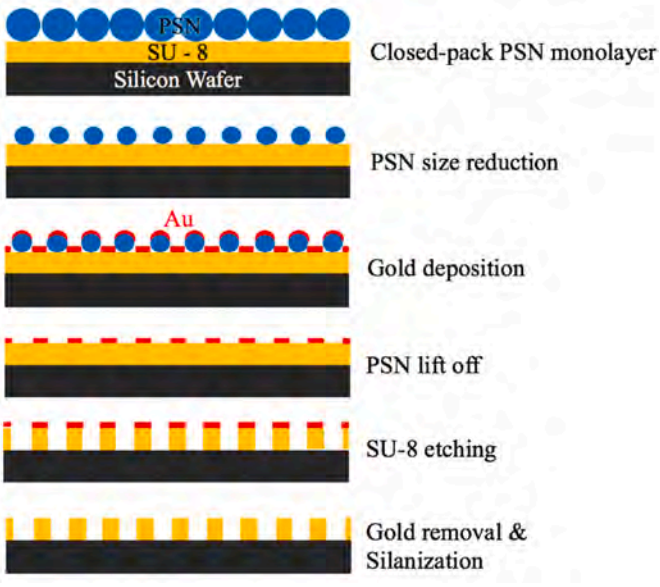


**Fig. 3.** Steps in the fabrication of master mask.

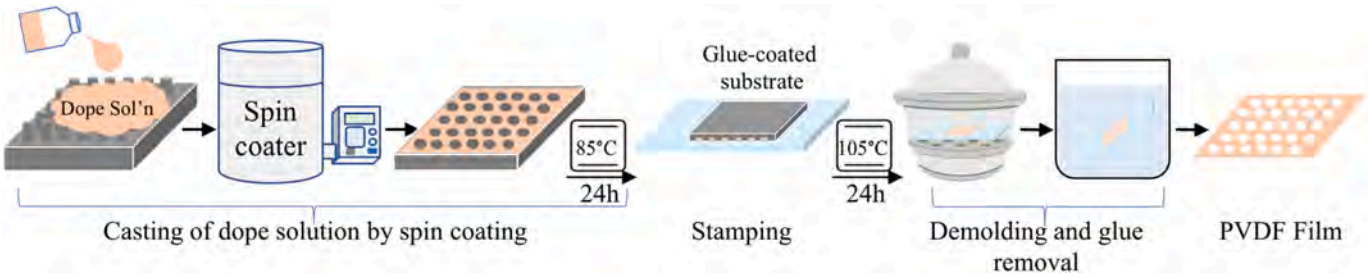


**Fig. 4.** Steps in fabricating PVDF nanomembrane using soft lithography.

**Step 3: Fabrication of the master mask**. The procedure for fabricating the master mask using PSN is shown in Fig. 3. The size of the PSN was controlled via reactive-ion etching (RIE) with oxygen plasma at aa RF power of 80W and a gas flow of 83 sccm. The size of the PSN was reduced from 300 nm to 100 nm and 20 nm (corresponding to the target pore sizes of the final nanomembrane) by varying the etching time. After reducing the PSN particle size, 5 nm layer of gold Au) was sputter-coated onto the surface using a vacuum sputter coater (Denton Vacuum Desk IV). The PSN was dissolved in toluene solution at 40 °C to partially open the SU-8 surface for RIE using the nanohole-patterned Au film as an etching mask. Next, the Au residue was removed from the SU-8 surface by wet etching with a commercially available gold etchant (TFA type) at an etch rate of 500 aA/min. Finally, the surface was silanized through low-pressure vapor deposition of FOTS under a gentle stream of nitrogen for 30 min. At each step in the fabrication process, a scanning electron microscope (JEOL JSM 6390) was used to observe the surface morphology of the mask.

**Step 4: Fabrication of isoporous nanomembrane by soft lithography**. The soft mold was made from polydimethylsiloxane (PDMS) purchased as a two-component package comprising a base and curing agent. Uncured PDMS was prepared by mixing its base and curing agent at 10:1 mass ratio. The mixture was vigorously stirred to ensure uniform distribution of the curing agent and then degassed under vacuum to release air bubbles. The PDMS solution was then poured onto the master and cured at 150 °C on a hot plate.

The procedure for fabricating the nanomembranes using the PDMS mold is shown in Fig. 4. The dope solution was prepared by dissolving polyvinylidene fluoride (PVDF) in N-Methyl-2-pyrrolidone (NMP) solution (18% w/w) and stirring continuously for 6 h at 85 °C, followed by sonication for 1 h. The stirring processes was restarted for another 24 h to ensure a homogenous solution, after which the stirring was stopped, and the dope solution was kept at 50 °C for another 24 h to release gas bubbles. The degassed dope solution was coated on the PDMS mold at room temperature using a spin coater (WS-400A-6NPP/LITE). The speed and spin duration of the spin coater were varied until the cast dope settled homogeneously into the channels of the mold and no residuals (dried excess dope) formed on the mold surface. A total of 7 repeated short cycles for the spin coating was performed to allow the dope to spread and set more evenly into the channels in the pattern. The resulting thin film was immediately dried at 85 °C for 24 h and then stamped onto a glass slide pre-coated with washable glue. The glass slide was dried at 105 °C for 24 h and cooled to room temperature in a desiccator before immersing overnight in ultrapure water. Finally, the membrane was stripped and air-dried at room temperature. Fourier transform infrared spectroscopy-attenuated total reflectance (FTIR-ATR) was employed to examine the crystalline structures of the product membrane.

**Evaluation of Membrane Properties and Performance Characteristics.** The nanocomposite membranes were analyzed under a scanning electron microscope (JSM JEOL 6390) to observe their surface morphology and pore characteristics. Tensile strength was measured at room temperature with a universal testing machine (Instron 5944) using a 2 cm × 4 cm membrane sample clamped at both ends and pulled at constant elongation speed of 0.1 mm/s. Hydrophobicity was measured via contact angle test using a high speed camera to capture the image of a 5 μL water drop on the membrane surface. Water flux was evaluated via bench-top dead-end and cross-flow filtration. Dead-end filtration was carried out using PVDF nanomembranes cut to size to fit in a 1-cm [2] filter holder with an opening of 10 $mm^2$. Cross-flow filtration was carried out using PVDF membranes cut to fit in a 16-cm [2] acrylic tangential flow filter holder with an effective flow area of 10 $cm^2$. Filtration tests were performed over 1 h at room temperature in duplicate runs, using a new membrane for each test run. In each filtration test, the feed solution was pumped through the filter using a peristaltic pump and permeate was collected over time. The permeate flux was calculated using the equation: $J_w = V_p/AT$, where $J_w$ is the permeate flux, $V_p$ is the volume of collected permeate, A is the membrane area, and T is the duration of sample collection. Rejection rates for PFOA and SMX were

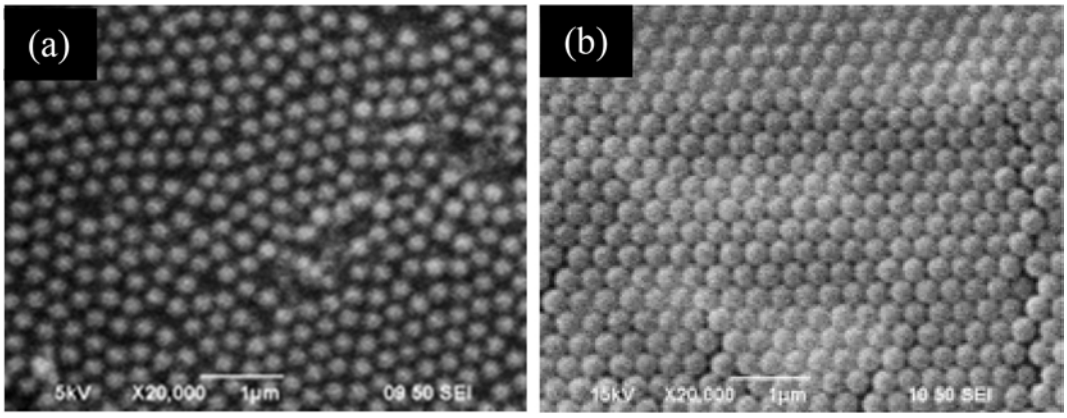


**Fig. 5.** SEM of polystyrene nanospheres (PSN) packing structure on a Su-8-coated silicon wafer. (a) dispersed PSN 2D array when PEO was not added (b) closely-packed PSN 2D array when PEO was added during PSN monolayer formation.

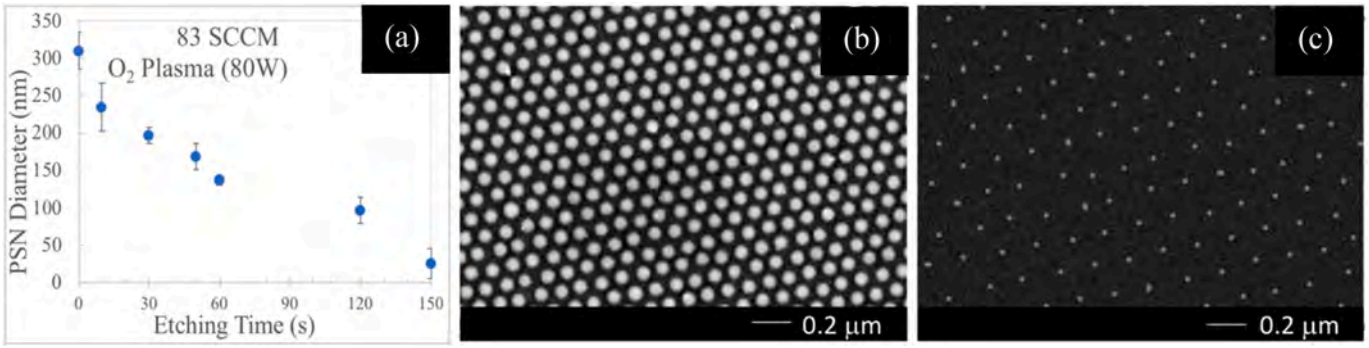


**Fig. 6.** Reactive-ion etching (RIE) process for polystyrene nanospheres (PSN) size control. (a) Reduction in diameter of PSN by RIE as function of etching time. (b) SEM of PSN layer etched for 120 s. (c) SEM of PSN layer etched for 150 s.

evaluated via cross-flow filtration carried out using aqueous solutions of 100 μg/L perfluorooctanoic acid (PFOA) and sulfamethoxazole (SMX) as feed. These filtration tests were performed in duplicate runs at room temperature in the dark, using a new membrane for each test run, and with each run lasting 36 h. The permeate was collected over time (every hour for the first 6 h, and every 3 h for the next 30 h) for chemicals analysis. The retentate was recycled back into the feed reservoir. PFOA and SMX concentrations were analyzed in a high-performance liquid chromatograph (Agilent 1260 Infinity II, DAD). Chromatographic separation was achieved with a C18 column (2.1 mm × 50 mm, 1.9 μm; Hypersil, Thermo Scientific) using isocratic flow (0.7 mL/min) of mobile phases consisting of 20 mM ammonium acetate and methanol (95:5, v/v). Limits of detection and quantification were taken at S/N = 3 and S/N = 10, respectively. Rejection rates for bovine serum albumin (BSA) and severe acute respiratory syndrome coronavirus 2 (SARS-CoV-2) were evaluated via dead-end filtration with membranes cut to fit a 13 mm filter holder with an opening of 78.5 mm2, and using spiked aqueous solutions of BSA (1 g/L) and heat-inactivated SARS-CoV-2 (100 gene copies/mL) as feed. The tests were performed in duplicate 3-hr runs, using a new membrane for each test run. The BSA in the permeate was analyzed using a UV–Vis spectrophotometer (HACH DR6000) at a wavelength of 278 nm.[16] For the SARS-CoV-2, 80 μL of viral RNA was isolated from the permeate using QIAamp Viral RNA kit (Qiagen) following manufacturer instructions. Viral load was quantified via RT-qPCR and targeting the N1 gene.[17].

## 3. Results and discussion

**Closely-packed PSN monolayer at the water-air interface.** Colloidal PSN float on the water-air interface and may aggregate due to van der Waals forces [18]. Slow dropwise addition of the PSN minimizes this aggregation and allows the PSN to self-assemble into a monolayer [19] of particles as the PSN cover the confinement area of the polypropylene ring. Nonetheless, without the addition of polyethylene oxide (PEO), these free-standing PSN are neither well-ordered nor closely packed (Fig. 5a). Competing repulsive and attractive forces between PSN give rise to this phenomenon. The surface charges of the PSN induce charged dipoles at the water-air interface, resulting in repulsive forces that cause a separation distance between particles, thus preventing closed packed self-assembly [15]. This separation distance decreases with increasing area fraction of PSN within the confinement area up to a certain fraction value at which the separation distance remains despite the addition of more PSN [18]. The presence of PSN at the interface can also induce attractive capillary forces, classified as a floating force (caused by particle weight) and an immersion force (due to capillary action) [15]. For large particles, surface tension generates greater curvature at the water-air interface to counter the weight of the particles [20]. The greater curvature provides more area for particle interactions, allowing them to form clusters even as they counter the horizontal pull

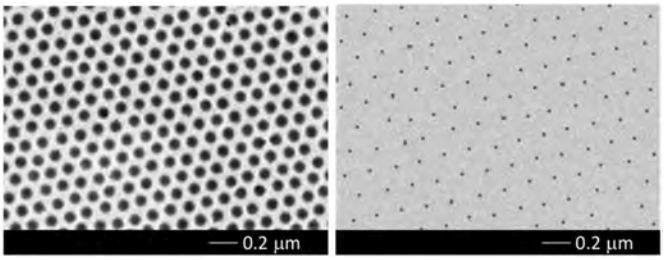


**Fig. 7.** Master mask fabricated by nanosphere lithographic technique: 100 nm (left) and 20 nm (right).

of surface tension [21]. However, if the particle is too small, the surface tension may not be able to generate enough attractive capillary force to draw in nearby PSN particles [22]. The addition of PEO greatly reduces surface tension at the interface, turning PSN movement to the lowest energy configuration [22]. This induces closer interparticle distance between PSN by increasing the attractive force between particles [18] and reducing the Brownian motion of individual particles or small PSN clusters [22]. The resulting closely-packed PSN monolayer is robust and maintains its structure without tearing even during subsequent transfer to a substrate. Fig. 5b shows the closely-packed PSN overlain on the SU-8-coated substrate, with a particle concentration of 1.21 × $10^9$ spheres/cm [2].

**Effect of RIE etching on the master mask structure.** Reactive ion etching (RIE) creates anisotropic etch profiles, thus it can be performed faster with greater precision than either physical ion bombardment or spontaneous chemical etching [23]. Here, RIE etching with oxygen

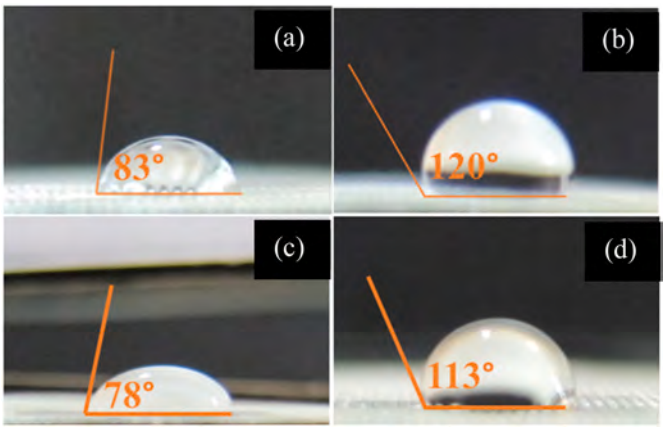


**Fig. 8.** Contact angles of the water droplet on the master mask surface for a 100-nm mask before (a) and after (b) silanization, and 20-nm mask before (c) and after (d) silanization with FOTS.

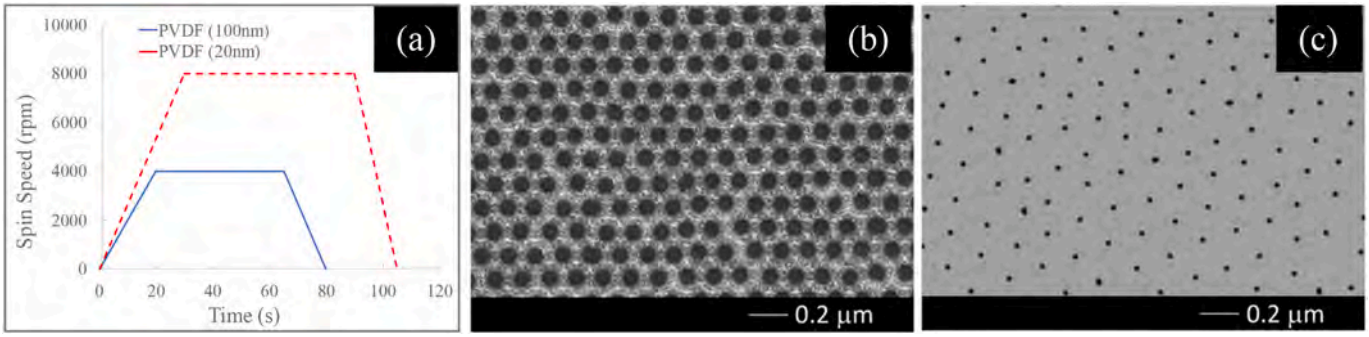


**Fig. 9.** Effect of spin process on PVDF membrane fabrication by soft lithography. (a) A single spin coating cycle plotted as a function of speed and time. (b) SEM image of PVDF membrane with 100 nm pores. (c) SEM image of PVDF membrane with 20- nm pores. SEM images of other sections of the larger membrane (see SI Figs. 1 and 2) show similar uniform pores.

plasma was used twice during mask fabrication, first to reduce the particle size of the PSN and thereby control the physical pitch of the final master mask, and second to etch the SU-8 surface after PSN is lifted along with the gold layer via wet etching with toluene. Fig. 6a shows the reduction of PSN diameter with increasing etching time at 80W of RF plasma power. 100 nm PSN (Figs. 6b) and 20 nm PSN (Fig. 6c) were obtained after 120 s and 150 s, respectively. The physical pitch of master mask pattern is determined from the starting PSN size, therefore it will be possible to obtain even smaller-pore nanomembranes with higher pore density and pore volume by using smaller-sized nanoparticles. Fig. 7 shows the SEM images of the master masks, indicating successful etching of highly structured uniform pores onto the SU-8 substrate for both 100 nm and 20 nm patterns.

Silanization with perfluorooctyltrichlorosilane (FOTS) improves the hydrophobicity of the mask surface, as indicated by goniometric measurements of the water droplet on the SU-8 surface before and after silanization (Fig. 8) [24]. Untreated SU-8 is highly hydrophobic but treatment with oxygen plasma increases its wettability [25] which can be problematic in subsequent polymer demolding steps. A silicon surface silanized with FOTS has lower surface energy at the interface [26] and can prevent the polymer from sticking to the mask during demolding.

**Effect of spinning technique on nanomembrane fabrication.** The dope solution was deposited on the center of the PDMS mold, then the mold was spun repeatedly over several brief spin cycles, with each cycle consisting of a ramp up period, a hold phase, and a deceleration period (Fig. 9a). These repeated spin cycles provide sufficient time for the dope solution to spread and settle into the mold channels more evenly compared to casting the solution in a single but long spin cycle. When fabricating PVDF thin films through spin coating, the spin speed and duration influence the rate at which the solvent evaporates from the film, which in turn affects how PVDF molecules settle and pack (i.e., coalesce [27]) into the mold channels. During this coalescence process, small PVDF molecules coalesce as the solvent evaporates, lowering the surface free energy needed to form a single entity (nucleus) [27,28]. This PVDF nucleus grows as it continues to draw in smaller PVDF molecules, leading to a continuous film with shorter separation distance between molecules [29], and thus a denser membrane with higher tensile strength [27]. Investigations on the spin cycles for the 100 nm pore membrane with an area of 16 $cm^2$ and 50 µm thick consisted of a ramp up to 4000 rpm in 20 s, followed by a 45 s hold, and the 20 s deceleration to stop. For the 20 nm pore membrane, the final cycle consisted of a ramp up to 8000 rpm in 30 s, then a 65 s hold, and deceleration to stop in 10 s. A total of seven repeated spin cycles was performed to successfully fabricate each isoporous nanomembrane. SEM images indicate a smooth surface, uniform and clean pores (no residual layers), and no tearing in the membranes (Fig. 9b and c).

PVDF is a thermoplastic polymer that has five crystalline forms (α, β, γ, δ and ε), with the predominance of the β form associated with higher PVDF crystallinity [30], polarity [31], mechanical strength [32], and increased antifouling performance [33]. Uniform PVDF films of various thickness have been successfully fabricated via spin coating, where the β-form in the films increased in content due to the simultaneous electric field poling [34] and stretching effect caused by the centrifugal force from the rotation [30]. In the present study, FTIR-ATR measurements

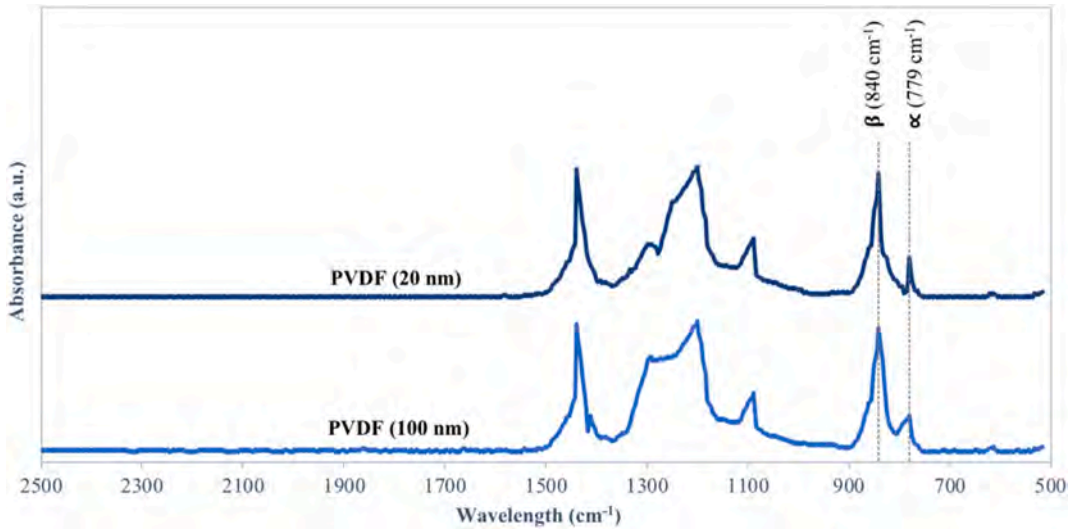


**Fig. 10.** Fourier transform infrared spectroscopy-attenuated total reflectance (FTIR-ATR) measurements for PVDF nanomembranes spun at 7 repeated cycles.

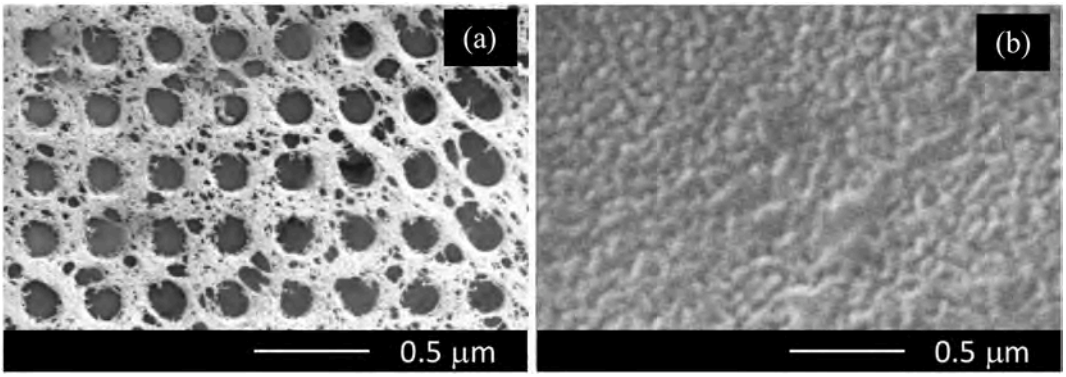


**Fig. 11.** Effect of other spin patterns on PVDF membranes: (a) membrane tearing due to higher spin speeds and (b) uneven membrane surface at slower spin speeds. (right).

**Table 1**
Characteristics of PVDF membranes fabricated using different techniques.

| Fabrication Technique | Tensile Strength (MPa) | Contact Angle | Water Flux (L/m$^2$h)/Filtration Set up | Configuration/Thickness (μm) | Average pore size from SEM (nm) | Ref |
|---|---|---|---|---|---|---|
| Electrospinning | 4.95 ± 1.36[b] | 127.80 ± 1.78°[c] | -[a] | Hollow fiber/160.5 ± 51.2 | 881.81 ± 156.80 | [43] |
| | 2.32 b | 121.3°[c] | 142.9/Dead-end filtration at 0.1 MPa | Flat sheet/-[a] | 1.56 | [44] |
| Phase Inversion | 1.62[b] | -[a] | 1026.7/Dead-end filtration at 0.1 MPa | Flat sheet/212.00 ± 8.34 | 367 | [45] |
| | 1.5[b] | 81.5°[c] | 600.0/Cross flow filtration at 0.05 MPa | Flat sheet/-[a] | 10.0–40.0 | [46] |
| Hybrid lithography | 8.56 ± 0.25[b] | 99.10 ± 1.56° | 2076.3 ± 1.2/Dead-end filtration at 0.1 MPa<br>2654.9 ± 4.0/Cross flow filtration at 0.1 MPa | Flat sheet/50.00 ± 5.21 | 100.46 ± 2.22 | This study |
| | 8.31 ± 0.02[b] | 100.80 ± 0.99° | 1676.2 ± 1.3/Dead-end filtration at 0.1 MPa<br>2603.4 ± 2.1/Cross flow filtration at 0.1 MPa | Flat sheet/50.00 ± 7.34 | 20.21 ± 0.80 | This study |

[d] via modified sessile drop test (see Methods section of this paper).
[a] Data not reported or measured in the reference;
[b] via ASTM D638;
[c] via sessile drop test;

(Fig. 10) indicate the predominance of the β-form (calculated relative abundance ratio of 0.51 and 0.52 for the 100-nm and 20-nm membranes, respectively) in the PVDF nanomembranes spun for 7 cycles, although β and α forms co-existed. Fewer cycles resulted in excessive PVDF residue and uneven membrane surface, while more cycles resulted in very thin membranes that tore during the demolding process.

At higher ramp up and hold spin speeds, the PVDF nanomembranes were found to be fragile and susceptible to tearing (Fig. 11a). For a hold spin speed of 9000 rpm, the calculated β fraction [30] from the FTIR measurements was 0.44, indicating non-predominance of the β crystalline form. Similar phenomenon was observed by Cardoso et al. [30] who noted that the crystallinity of spun PVDF films decreased with increased spin speed due to limitations in the formation of the β-form, which depended on the viscosity of the PVDF solution. Low rotational speeds in spin coating have been shown to cause slower evaporation of the solvent and thus longer late stage crystallization and larger crystalline domains in the final solid film structure [29]. This work also observed thicker and uneven membrane surfaces at lower spin speeds (Fig. 11b).

**Mechanical Properties and Performance Characteristics of PVDF Nanomembranes.** PVDF nanomembranes with tensile strengths of 2.4–4.95 MPa have been successfully used in gas separation [35], pharmaceutical purification [36], and desalination [37]. The effects of surface properties such as roughness, wettability, and surface charges on the membrane's permeability, rejection rate, and antifouling ability are also well documented [38]. Contaminants accumulate on uneven membrane surface, promoting clogging that increases fouling and reduces flux [39]. The membrane's wettability and surface charges influence attractive or repulsive surface interactions with contaminants, which can lead to fouling and clogged pores [40]. Current methods for improving the mechanical and surface properties of PVDF membranes include physical (manufacturing) and chemical approaches (surface modifications and use of additives) [41,42].

This study focused on process design to improve membrane properties, where our hybrid nano and soft lithography techniques resulted in the product membranes' even surface and high permeability. The tensile strength, wettability, and water flux (for cross and dead-end filtration) of the fabricated PVDF nanomembranes are summarized in Table 1, along with similar literature data for comparable membranes manufactured via electrospinning and phase inversion. The 100 nm and 20 nm nanomembranes fabricated by hybrid lithography have comparatively higher tensile strength despite their relatively lower thickness which we relate with the formation of the β phase. Both are hydrophobic, with water contact angles of 99.1 ± 1.6° and 100.8 ± 0.9°, respectively. The contact angle and water flux for the 100 nm membrane are comparable to the PVDF membrane fabricated via phase inversion and with similar nominal pore size. Of note is the high uniformity of the pore size of membranes fabricated via hybrid lithography (SI Figs. 1 and 2), which has significantly low variability compared to other membranes manufactured via other techniques.

Fig. 12 shows the flux and rejection rates for aqueous solutions (100 μg/L) of perfluorooctanoic acid (PFOA) and sulfamethoxazole (SMX) via cross-flow filtration conducted in the dark. Both 100-nm and 20-nm

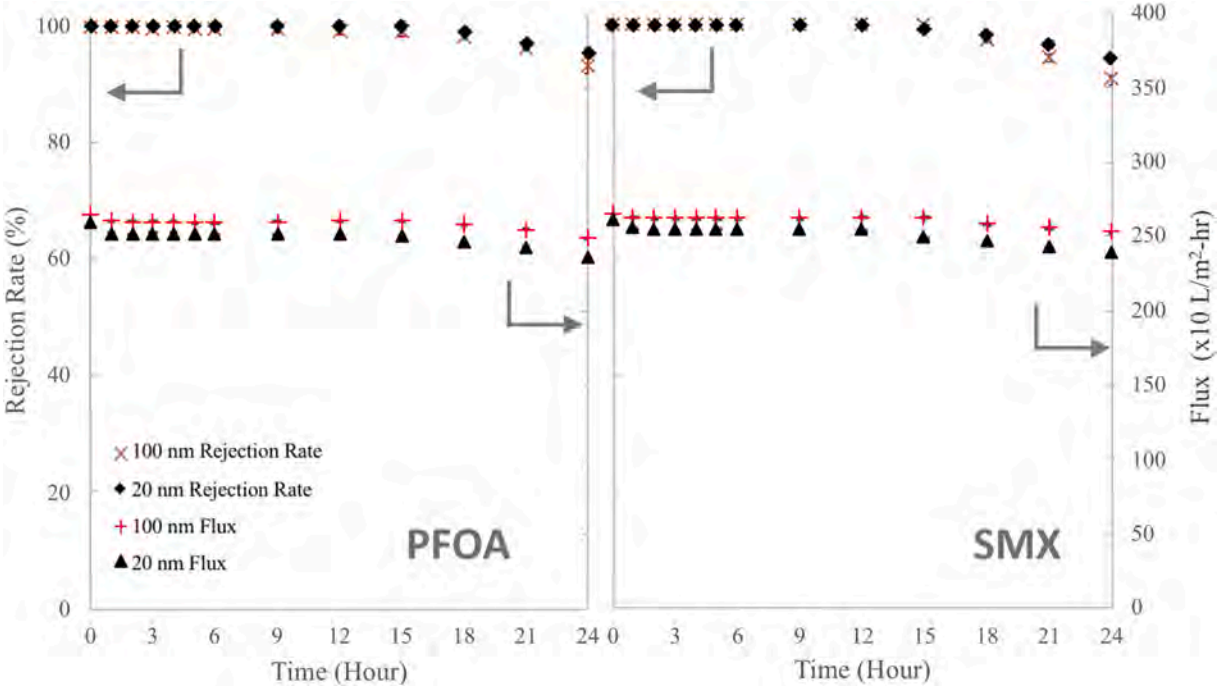


**Fig. 12.** Flux and rejection rates for 100 μg/L aqueous solutions of perfluorooctanoic acid (PFOA) and sulfamethoxazole (SMX) via cross-flow filtration with 100-nm and 20-nm PVDF membranes.

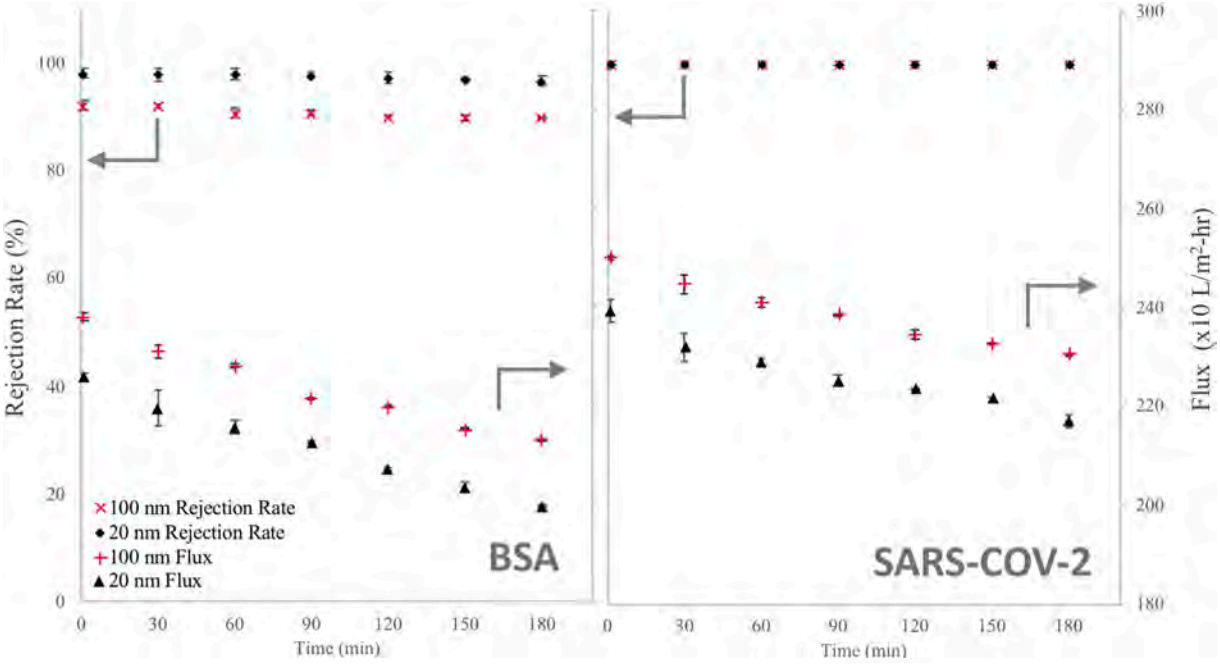


**Fig. 13.** Flux and rejection rates for solutions of bovine serum albumin (BSA, 1 g/L) and heat-inactivated SARS-CoV-2 (100 gene copies/mL) via dead-end filtration with 100-nm and 20-nm PVDF membranes.

membranes exhibited steady high flux followed by gradual decline in flux after 15 h and 12 h, respectively, of continuous operation. Flux declined by only 0–4% after 24 h of continuous operation (no back-washing). Steady flux periods were accompanied by 100% rejection rates for PFOA and SMX. After 24 h, rejection rates for PFOA and SMX were 93% and 91%, respectively, with the 100 nm membrane. For the same period, rejection rates for PFOA and SMX were 95% and 94%, respectively with the 20 nm membrane. Flux drops were relatively higher for BSA and SARS-CoV-2 (Fig. 13) likely due to their larger molecular sizes. BSA has a nominal size of 8 nm though aggregation can increase particle size to 300 nm[47]; the estimated nominal size for SARS-CoV-2 is 120 nm[48]. After 3 h, rejection rates for BSA were 90% and 97%, respectively, for the 100 nm and 20 nm membranes. 100% rejection rates for SARS-CoV-2 were observed in both membranes. The highly ordered pore structures in isoporous membranes result in high permeability and rejection rates, making these membranes ideal for various specialized applications such as in water treatment [49], drug delivery [50], protein separation [51], biosensing [9], and in personal

protective equipment [52].

**Advantages of Hybrid Lithography Method.** Lithography-based techniques offer simple, cost-efficient, and greener routes [13] for manufacturing membranes with high pattern resolution [53] but creation of the master mask, though done only once, can increase manufacturing costs [54] when done via conventional lithography. The present work addresses this limitation by eliminating the use of expensive and complex instrumentation (e-beam lithography) and stringent laboratory environment controls (clean room), making it more economically-appealing with potential for expansion to large scale production. Our simple 4-step process excels at making uniform and periodic 100-nm and 20-nm pore membranes with a 50 μm nominal thickness that exhibit high strength due to improved β crystalline formations of the PVDF. Our useful fabrication procedure is compatible with developed technologies that can quickly expand the opportunities of isoporous PVDF for processing of advanced materials and devices. Once fabricated, the soft mold can be repeatedly used for fabricating membranes. Due to the high elasticity, flexibility, and hydrophobicity of the PDMS, it is easy to fabricate the mold using the SU-8 mask while maintaining the integrity of the pattern in the final mold. Silanizing the master mask induces its surface hydrophobicity, thus preventing the PDMS mold from sticking to the mask. So long as the mask and the mold are kept clean in between pattern transfers, the integrity of the pattern is preserved. We have successfully produced several membranes with the mold without significant defects detected. Furthermore, the key steps of the fabrication process can be readily modified to make them suitable for web-based roll-to-roll (R2R) manufacturing process.

## 4. Conclusions

In the present work we developed a simple and rapid procedure for fabricating isoporous thin film PVDF nanomembranes using hybrid nanolithography and soft lithography. Reactive plasma was used to etch the mask from a monolayer of nanosphere particles and to transfer the pattern on an elastomeric mold. The mold was then used to cast nanomembrane films with uniform 100 nm and 20 nm through pores. The membranes exhibited high tensile strength, permeability, hydrophobicity, and rejection rates for PFOA, SMX, BSA, and SARS-CoV-2. The developed fabrication method does not require the use of high energy laser (for etching) nor a clean room (for mask fabrication), making the process low cost with potential for large scale industrial application. It may also be feasible to adapt these hybrid lithography techniques into roll-to-roll technology, where the pattern stamp on the R2R reel is manufactured using nanolithography (for the mask) and soft lithography (for the embedded stamp).

## Declaration of competing interest

The authors declare that they have no known competing financial interests or personal relationships that could have appeared to influence the work reported in this paper.

## Acknowledgment

This research was supported by funding from the University of Massachusetts Lowell Office of Research Administration (R50170000035648). The authors thank Jack Lepine for assistance in RT-qPCR analysis for SARS-CoV-2, Polnop Samutpraphoot for assistance in RIE etching, Dr. Jin Xu for providing HPLC access, Dr. Therrien Joel and Michael Masaki for their assistance in performing FTIR measurements, and Dr. Earl Ada for his assistance in processing and analyzing SEM images.

## Appendix A. Supplementary data

Supplementary data to this article can be found online at https://doi.org/10.1016/j.polymertesting.2021.107316.

## Author contributions

AR performed the experiments and data analysis, and contributed in manuscript writing. SP contributed in experimental design, data analysis, and manuscript writing and review. JP and HS contributed in experimental design and manuscript review.

## References

[1] C.Y. Lai, A. Groth, S. Gray, M. Duke, Nanocomposite for improved physical durability of porous PVDF membranes, Membranes 4 (2014) 55–78.
[2] Y. Liao, C.H. Loh, M. Tian, R. Wang, A.G. Fane, Progress in electrospun polymeric nanofibrous membranes for water treatment: fabrication, modification and applications, Prog. Polym. Sci. 77 (2018) 69–94.
[3] L. Madauß, J. Schumacher, M. Ghosh, O. Ochedowski, J. Meyer, H. Lebius, B. Band'Etat, M.E. Toimil-Molares, C. Trautmann, R.G. Lammertink, M. Ulbricht, M. Schleberger, Fabrication of nanoporous graphene/polymer composite membranes, Nanoscale 9 (29) (2017) 10487–10493.
[4] K.T. Tran, T.D. Nguyen, Lithography-based methods to manufacture biomaterials at small scales, J. Sci.: Adv Mat Devices 2 (1) (2017) 1–14.
[5] H. Bessbousse, M. Barsbay, O. Guven, M.C. Clochard, T.L. Wade, Functionalized nanoporous track-etching β-PVDF membrane electrodes for heavy metal determination by square-wave anodic stripping voltammetry, Anal Methods 3 (2011) 1351–1359.
[6] F.E. Admed, B.S. Lalia, R. Hashaikeh, A review on electrospinning for membrane fabrication: challenges and applications, Desalination 356 (2015) 15–30.
[7] M.G. Buonomenna, P. Macchi, M. Davoli, E. Drioli, Poly(vinylidene fluoride) membranes by phase inversion: the role the casting and coagulation conditions plat in their morphology, crystalline structure and properties, Eur. Polym. J. 43 (2007) 1557–1572.
[8] E. Ferain, R. Legras, Pore shape control in nanoporous particle track etched membrane, Nucl. Instrum. Methods Phys. Res., Sect. B 174 (2001) 116–122.
[9] A. Sabirova, F.J. Pisig, N. Rayapuram, H. Hirt, S.P. Nunes, Nanofabrication of isoporous membranes for cell fractionation, Sci. Rep. 10 (2020) 6138.
[10] S. Agarwal, A. Greiner, J.H. Wendorff, Functional materials by electrospinning of polymers, Prog. Polym. Sci. 38 (6) (2013) 963–991.
[11] S.K. Nune, K.S. Rama, V.R. Dirisala, M.Y. Chavali, Electrospinning of collagen nanofiber scaffolds for tissue repair and regeneration, in: D. Ficai, A. M. Grumezescu (Eds.), Nanostructures for Novel Therapy, Elsevier, 2017, pp. 281–311.
[12] S. Remanan, M. Sharma, S. Bose, N.C. Das, Recent advances in preparation of porous polymeric membranes by unique techniques and mitigation of fouling through surface modification, Chem Select 3 (2018) 609–633.
[13] Z. Nie, E. Kumacheva, Patterning surfaces with functional polymers, Nat. Mater. 7 (2008) 277–290.
[14] K.C. Noh, M.D. Oh, S.C. Lee, A numerical study on airflow and dynamic cross-contamination in the super cleanroom for photolithography process, Build. Environ. 40 (11) (2005) 1431–1440.
[15] P.H. Lei, C.-D. Yang, Y.-S. Yang, J.-H. Lin, Preparation of a periodic polystyrene nanosphere array using the dip-drop method with post-deposition etching and its application of improving light extraction efficiency of InGaN/GaN LEDs, Nanoscale Res Lett 13 (2018) 180–189.
[16] V.D. Suryawanshi, L.S. Walekar, A.H. Gore, P.V. Anbhule, G.B. Kolekar, Spectroscopic analysis on the binding interaction of biologically active pyrimidine derivative with bovine serum albumin, J Pharma Anal 6 (1) (2016) 56–63.
[17] United States Center for Disease Control. CDC 2019-Novel Coronavirus (2019-nCoV) Real-Time RT-PCR Diagnostic Panel. CDC-006-00019, Revision: 06.
[18] C.-C. Ho, P.-Y. Chen, K.-H. Lin, W.-T. Juan, W.-L. Lee, Fabrication of monolayer of polymer/nanospheres hybrid at a water-air interface, ACS Appl. Mater. Interfaces 3 (2011) 204–208.
[19] A. Qdemat, E. Kentzinger, J. Buitenhuis, U. Rucker, M. Ganeva, Bruckel, Self assembled monolayer of silica nanoparticles with improved order by drop casting, RSC Adv. 10 (2020) 18339–18347.
[20] A. Chandramohan, N.V. Sibirev, V.G. Dubrovskii, V.G. Petty, A.J. Gallant, D. A. Zeze, Model for large-area monolayer coverage of polystyrene nanospheres by spin coating, Sci. Rep. 7 (2017) 40888–40896.
[21] J. Shang, M. Flurry, Y. Deng, Force measurements between particles and the air-water interface: implications for particle mobilization in unsaturated porous media, Water Resour. Res. 45 (2009) 1–14.
[22] C. Zhang, S. Cvetanovic, J.M. Pearce, Fabricating ordered 2D nano-structured arrays using nanosphere lithography, Methods (Duluth) 4 (2017) 229–242.
[23] S.M. Sze, M.-K. Lee, Semiconductor Devices: *Physics And Technology*, John Wiley & Sons, 2012.
[24] M. Ikawa, T. Yamada, H. Matsui, H. Minemawari, J. Tsutsumi, Y. Horii, M. Chikamatsu, R. Azumi, R. Kumai, T. Hasegawa, Simple push coating of polymer thin-film transistors, Nat. Commun. 3 (2012) 1176.
[25] F. Walther, P. Davydovskaya, S. Zürcher, M. Kaiser, H. Herberg, A.M. Gigler, R. W. Stark, Stability of the hydrophilic behavior of oxygen plasma activated SU-8, J Microcmech Microeng 17 (3) (2017) 524.

[26] O.P. Khatri, D. Devapprakasam, S.K. Biswas, Frictional responses of Octadecyltrichlorosilane (OTS) and 1H, 1H, 2H, 2H-Perfluorooctyltrichlorosilane (FOTS) monolayers self-asse, Tribology 20 (2005) 235.
[27] M. Li, I. Katsouras, C. Piliego, G. Glasser, I. Lieberwirth, P.W.M. Blom, D.M. De Leeuw, Controlling the microstructure of poly(vinylidenefluoride)(PVDF) thin films for microelectronics, Mater. Chem. C 1 (2013) 7695–7702.
[28] A.A. Ribeiro, R.F.C. Marques, G.A. Carlos, J.S.d.C. Campos, Hydroxyapatite deposition study through polymeric process on commercially pure Ti surfaces modified by laser beam irradiation, J. Mater. Sci. 44 (2009) 4056–4061.
[29] K.W. Chou, H.U. Khan, M.R. Niazi, B. Yan, R. Li, M.M. Payne, J.E. Anthony, D.-M. Smilgies, A. Amassian, Late stage crystallization and healing during spin-coating enhance carrier transport in small-molecule organic semiconductors, J. Mater. Chem. C 2 (2014) 5681–5689.
[30] V.F. Cardoso, G. Minas, S. Lanceros-Méndez, Multilayer spin-coating deposition of poly (vinylidene fluoride) films for controlling thickness and piezoelectric response, Sens. Actuators, A 192 (2013) 76–80.
[31] A.M. Varposhti, M. Yousefzadeh, E. Kowsari, M. Latifi, Enhancement of β-phase crystalline structure and piezoelectric properties of flexible PVDF/ionic liquid surfactant composite nanofibers for potential application in sensing and self-powering, Macromol. Mater. Eng. 305 (2020) 1900796.
[32] J. Liu, X. Lu, C. Wu, Effect of preparation methods on crystallization behavior and tensile strength of poly(vinylidene fluoride) membranes, Membranes 3 (2013) 389–405.
[33] Y. Zhang, L. Ye, W. Zhao, L. Chen, M. Zhang, G. Yang, H. Zhang, Antifouling mechanism of the additive-free β-PVDF membrane in water purification process: relating the surface electron donor monopolarity to membrane-foulant interactions, J. Membr. Sci. 601 (2020) 117873.
[34] L. Ruan, X. Yao, Y. Chang, L. Zhou, G. Qin, X. Zhang, Properties and applications of the β phase poly (vinylidene fluoride), Polymers 10 (2018) 228.
[35] E.A. Feijani, A. Tavasoli, H. Mahdavi, Improving gas separation performance of poly(vinylidene fluoride) based mixed matrix membranes containing metal–organic frameworks by chemical modification, Ind. Eng. Chem. Res. 54 (2015) 12124–12134.
[36] F. Boschin, N. Blanchemain, M. Bria, E. Delcourt-Debruyne, M. Morcellet, H. F. Hidebrand, B. Martel, Improved drug delivery properties of PVDF membranes functionalized with beta-cyclodextrin–application to guided tissue regeneration in periodontology, J. Biomed. Mater. Res. 79 (2006) 78–85.
[37] H. Fan, Y. Peng, Application of PVDF membranes in desalination and comparison of the VMD and DCMD processes, Chem. Eng. Sci. 79 (2012) 94–102.
[38] M. Amirilargani, M. Sadrzadeh, E. Sudholter, L.D. Smet, Surface modification methods of organic solvent nanofiltration membranes, Chem. Eng. J. 289 (2016) 562–582.
[39] E.M. Vrijenhoek, S. Hong, M. Elimelech, Influence of membrane surface properties on initial rate of colloidal fouling of reverse osmosis and nanofiltration membranes, J. Membr. Sci. 188 (2001) 115–128.
[40] H. Nagasawa, T. Omura, T. Asai, M. Kanezashi, T. Tsuru, Filtration of surfactant-stabilized oil-in-water emulsions with porous ceramic membranes: effects of membrane pore size and surface charge on fouling behavior, J. Membr. Sci. 610 (2020) 118210.
[41] L. Shen, S. Feng, J. Li, J. Chen, F. Li, H. Lin, G. Yu, Surface modification of polyvinylidene fluoride (PVDF) membrane via radiation grafting: novel mechanisms underlying the interesting enhanced membrane performance, Sci. Rep. 7 (2017) 1–13.
[42] J.P. Mericq, J. Mendret, S. Brosillon, C. Faur, High performance PVDF-TiO2 membranes for water treatment, Chem. Eng. Sci. 123 (2015) 283–291.
[43] Y. Zhang, B. Yang, K. Li, D. Hou, C. Zhao, J. Wang, Electrospun porous poly (tetrafluoroethylene-cohexafluoropropylene- co-vinylidene fluoride) membranes for membrane distillation, RSC Adv. 7 (2017) 56183.
[44] S. Gopi, R. Kargl, K.S. Kleinschek, A. Pius, S. Thomas, Chitin nanowhisker–Inspired electrospun PVDF membrane for enhanced oil-water separation, J Envi Mngt 228 (2018) 249–259.
[45] Z. Cui, Y. Cheng, K. Xu, J. Yue, Y. Zhou, X. Li, Q. Wang, S.-P. Sun, Y. Wang, X. Wang, Z. Wang, Wide liquid-liquid phase separation region enhancing tensile strength of poly(vinylidene fluoride) membranes via TIPS method with a new diluent, Polymer 141 (2018) 46–53.
[46] I.A. Ike, J. Zhang, A. Groth, J.D. Orbell, M. Duke, Effects of dissolution conditions on the properties of PVDF ultrafiltration membranes, Ultrason. Sonochem. 39 (2017) 716–726.
[47] K.J. Hwang, P.Y. Sz, Effect of membrane pore size on the performance of cross-flow microfiltration of BSA/dextran mixtures, J. Membr. Sci. 378 (1–2) (2011) 272–279.
[48] Y.M. Bar-On, A. Flamholz, R. Phillips, R. Milo, Science forum: SARS-CoV-2 (COVID-19) by the numbers, Elife 9 (2020), e57309.
[49] Y.K. Choi, S.M. Park, S. Lee, D.-Y. Khang, D.-C. Choi, C.-H. Lee, Characterization and theoretical analysis of isoporous cycloaliphatic polyurethane membrane for water treatment, Desalination Water Treat 52 (2013) 1021–1027.
[50] M.E. Warkiani, A.A.S. Bhagat, B.L. Khoo, J. Han, C.T. Lim, H.Q. Gong, A.G. Fane, Isoporous micro/nanoengineered membranes, ACS Nano 7 (2013) 1882–1904.
[51] J. Hahn, J.I. Clodt, V. Filiz, V. Abetz, Protein separation performance of self-assembled block copolymer membranes, RSC Adv. 4 (2014) 10252.
[52] A. Sabirova, S. Wang, G. Falca, P.Y. Hong, S.P. Nunes, Flexible isoporous air filters for high-efficiency particle capture, Polymer 213 (2021) 123278.
[53] D. Qin, Y. Xia, G.M. Whitesides, Soft lithography for micro- and nanoscale patterning, Nat. Protoc. (2010) 5491–5502.
[54] R.M.M. Hasan, X. Luo, Promising lithography techniques for next-generation logic devices, Nanomanufac Metrol 1 (2018) 67–81.